Acta Polytechnica CTU Proceedings **55**:89–100, 2025
https://doi.org/10.14311/APP.2025.55.0089

Published by the Czech Technical University in Prague

THERMAL DIFFUSIVITY OF ATF CLADDING MATERIALS USING LASER FLASH TECHNIQUE

Jakub Vrzal[a, b, *], Martin Ševeček[a], Luka Vlahovic[b]

[a] *Czech Technical University in Prague, Faculty of Nuclear Sciences and Physical Engineering, Department of Nuclear Reactors, V Holešovičkách 2, 180 00 Prague 8, Czech Republic*

[b] *European Commission, Joint Research Centre, Institute for Transuranium Elements, P.O. Box 2340, 76125 Karlsruhe, Germany*

[*] corresponding author: vrzalja1@cvut.cz

Abstract. Accident tolerant fuel (ATF) cladding materials are designed to improve the fuel behavior in normal operation while further enhancing the material performance in accidental scenarios. The paper presents experimental data on thermal diffusivity for five advanced cladding candidates considered as ATFs, evaluated over a wide temperature range using the laser flash technique. The measured data were evaluated to identify trends in thermophysical behavior in the investigated temperature range. Based on the results, correlations were established to describe the temperature dependence of thermal diffusivity for each material. The analysis also revealed characteristic differences in the thermal diffusivity for various candidates. These findings provide a comparative perspective on the heat transfer capabilities of the tested materials and offer a fundamental experimental basis for their further optimization in accident tolerant fuel applications.

Keywords: Accident tolerant fuel, cladding, laser flash technique, thermal diffusivity, SiC, FeCrAl.

1. Introduction

Conventional zirconium-based cladding materials exhibit rapid high-temperature oxidation and significant hydrogen release during Loss-of-Coolant accidents (LOCAs) and beyond design basis accidents, leading to exothermic runaway reactions that threaten reactor or containment integrity. This has driven worldwide initiatives to develop accident-tolerant cladding options, such as coated Zr alloys, FeCrAl alloys, and SiC-based composites, which significantly reduce oxidation rates as well as accompanying hydrogen release, thus providing additional coping time during severe accidents [1–3].

Beyond accident resilience, ATF materials are also expected to equal or exceed conventional claddings in terms of thermophysical and mechanical behavior during nominal operation. Properties such as thermal conductivity, heat capacity, and thermal diffusivity are critical to achieve efficient heat removal from the fuels, maintain temperature control, and ensure structural integrity. Enhanced thermophysical performance not only improves day-to-day safety margins but also supports long-term durability and fuel efficiency [3].

Thermal diffusivity (α) quantifies the rate at which heat diffuses through a material and is given by the ratio of thermal conductivity to volumetric heat capacity ($\alpha = \frac{\lambda}{\rho c_p}$). Although not always a dominant parameter, accurate knowledge of α contributes to informing and improving thermal simulations, better material characterization, and more reliable safety analyses. Laser Flash analysis (LFA), introduced by Parker et al. (1961) [4] and further developed by Magli and Taylor (1989) [5], is a well-established technique for measuring α over a wide temperature range due to its non-contact operation, high speed, and precision. Its compatibility with thin disk-shaped specimens makes it particularly suitable for evaluating advanced cladding materials [4, 5].

The paper is organized as follows. Section 2 provides a detailed description of the selected five ATF cladding candidate materials: FeCrAl B136Y3, SiC CTP, SiC NITE, ADSS #B51, and 42XNM. Section 3 outlines the experimental methodology, including the Laser Flash Technique used for thermal diffusivity measurements. Section 4 presents the measurement results and the correlations derived, highlighting the temperature dependence of the thermal behavior of the materials studied.

2. Materials and methods

2.1. Overview of investigated ATF cladding materials

This section provides a summary of all accident tolerant fuel (ATF) cladding materials selected for experimental evaluation in this study. The investigated materials include metallic alloys and ceramic-based composites, each with distinct structural, thermal, and corrosion-resistant characteristics relevant to light-water reactor (LWR) applications. These materials were either manufactured at CTU in Prague or provided by international partners such as KAIST, KIT, CTP, and NITE.

The evaluated materials comprise two iron-based alloys (ADSS # B51 and FeCrAl B136Y3), one high-

chromium nickel alloy (42XNM), and two SiC-based claddings produced using different fabrication techniques and with very different designs (CTP and NITE).

2.1.1. High aluminum duplex stainless steels (ADSS #B51)

The primary focus during the design of the ADSS alloy system done at Korea advanced Institute of Science and Technology Korea (KAIST), was to optimize the balance of Ni, Cr, and Al to achieve a favorable combination of phase stability, mechanical performance, and corrosion resistance. Nickel acts as an austenite stabilizer, promoting the formation of a face-centered cubic (FCC) phase, which contributes to the mechanical strength and toughness of the alloy. Chromium, on the other hand, stabilizes the ferritic phase (BCC) and supports the formation of a protective oxide layer that improves corrosion resistance. To ensure a balanced duplex microstructure, we chose the weight fractions of Cr and Ni to be similar; however, a lower Ni content is preferred to enhance irradiation tolerance. Furthermore, a minimum of 5 wt.% aluminum was selected to allow the formation of a stable α-Al_2O_3 scale at high temperatures, while avoiding excessive embrittlement that could result from too high Al content [6].

To identify the optimal phase constitution, a series of thermodynamic calculations were performed at 900 °C, evaluating the phase fractions as a function of the Ni and Al content, for two Cr levels (16 and 21 wt.%). Based on these calculations, specific alloy compositions were selected that exhibit a desirable duplex microstructure with a controlled fraction of the intermetallic B2-NiAl phase. As a result, several alloy variants were identified for further investigation, including #B11, #B22, #B32, and #B51. The exact composition data are presented in Table 1 [6].

Alloy (wt.%)	Fe	Ni	Cr	Al	Nb	Mn	Si	C
ADSS#B11	Bal.	18.3	16.2	4.93	1.39	1.22	0.34	0.11
ADSS#B22	Bal.	20.6	16.3	5.36	1.58	1.08	0.36	0.12
ADSS#B32	Bal.	21.4	20.9	5.50	0.52	1.04	0.32	0.12
ADSS#B51	Bal.	18.7	16.3	6.14	0.53	1.04	0.31	0.11
ADSS#B51	Bal.	19.2	16.76	5.84	0.33	0.84	0.11	0.09

Table 1. Chemical composition of ADSS alloys developed at KAIST [6].

2.1.2. FeCrAl B136Y3

FeCrAl alloys, including B136Y3, are being considered as ATF cladding materials due to their excellent oxidation resistance and mechanical properties. The designation B136Y3 refers to a second-generation FeCrAl alloy, where the name reflects its specific composition. The detailed chemical composition, together with other representative FeCrAl alloys, is provided in Table 2. The material was manufactured by Oak Ridge National Laboratory and provided to Karlsruhe Institute of Technology (KIT) for the QUENCH-19 experiment. The cladding tested was segmented from a low-temperature part of the QUENCH-19 experiment and kindly provided to CTU by KIT. The high Cr and Al content allows the formation of a stable protective oxide layer, resulting in over 100 times lower oxidation rates in steam at high temperatures compared to zirconium alloys, which also results in lower hydrogen generation during exposure to high temperature [7–9].

Alloy (wt.%)	Fe	Cr	Al	Mo	Y	C	Si	Mn
APM	Bal.	20.5–23.5	5.8	–	–	<0.08	<0.7	<0.4
APMT		20.5–23.5	5.0	3.0	–	<0.08	<0.7	<0.4
B136Y3		12.97	6.19	–	0.03	<0.01	–	–
C06M		10	6.00	2.0	0.05	<0.01	0.2	–
C36M		13	6.00	2.0	0.05	<0.01	0.2	–

Table 2. Chemical composition of selected FeCrAl-based alloys [9].

However, its higher thermal neutron absorption negatively impacts the neutron economy. This may require thinner cladding or enriched fuel to maintain performance. Another drawback relevant to Boiling water reactors (BWRs) is the higher permeability of tritium due to imperfect sealing, which poses a concern given the design of the BWR primary circuit [8].

Thermophysical data for B136Y3 are limited, but based on its compositional similarity to C36M, it is expected to have higher specific heat but lower thermal conductivity and diffusivity than Zircaloy-4. Despite these trade-offs, B136Y3 remains a viable candidate for BWR ATF applications [10].

2.1.3. SiC CTP

The SiC CTP cladding is based on a three-layer SiC/SiC architecture. The inner layer consists of a highly dense SiC monolith that serves as the primar l ad-bearing structure. The intermediate layer is a composite made of SiC fibers embedded in a SiC matrix, providing improved toughness and crack resistance. The outer layer is a thin environmental barrier coating (OB). Although all layers are composed of silicon carbide, each is manufactured by a different processing method, resulting in distinct material properties [11].

The SiC CTP cladding was provided by CTP USA. Unfortunately, due to the proprietary nature of the design and its commercial development, detailed information about composition, structure, and thermomechanical properties is limited [11].

Despite the lack of detailed data, SiC-based composites are promising ATF candidates, particularly because of their exceptional high-temperature oxidation resistance, mechanical strength, and negligible hydrogen generation. These properties are of particular interest for BWR applications, where steam exposure is critical. However, the lack of detailed thermophysical property data remains a barrier to a full assessment [8, 11].

2.1.4. SiC NITE

Another SiC-based cladding considered in this work is SiC-NITE, named after the nano-infiltrated transient eucalyptus (NITE) processing technique. This method produces a highly dense SiC matrix reinforced with polycrystalline SiC fibers, which are effectively protected during sintering, cooling, and other manufacturing steps that could otherwise degrade the integrity of the composite. The NITE process not only prevents material degradation during the processing, but also improves the mechanical properties of the cladding. In addition, it offers geometric flexibility, making it adaptable for the production of fuel cladding [12, 13].

In this study, a NITE cladding developed by NITE Corporation is used. It consists of Hi-Nicalon Type S polycrystalline fibers coated with CVD carbon embedded in a NITE-SiC matrix with very low porosity. SiC-NITE cladding offers excellent potential for advanced ATF systems, especially in BWR reactors, due to its chemical stability in steam, minimal hydrogen generation, and mechanical resilience. However, the lack of openly available thermophysical data remains a limitation for a comprehensive evaluation [12, 13].

2.1.5. Cr-Ni alloy 42XNM

Another candidate investigated in this study is the 42XNM alloy (also known as 42KhNM, depending on the source), a chromium-nickel-based material developed in former Soviet Union, which is now a promising ATF cladding candidate. Unlike conventional Cr-Ni steels, typically composed in an 80:20 ratio, 42XNM features a distinctly different composition of approximately 42 wt.% Cr, 1.5 wt.% Mo, and aluminum additions. The alloy demonstrates excellent corrosion resistance, even under high-temperature steam exposure, and does not react with water, making it an attractive candidate for accident tolerant fuel designs. In contrast to conventional austenitic steels, 42XNM is also resistant to stress corrosion cracking. Oxidation tests conducted at 1 200 °C have shown that 42XNM forms significantly thinner oxide layers, up to 20 times less than those formed in the zirconium alloy E110 under identical conditions [14, 15].

However, the alloy presents some drawbacks that must be considered in reactor applications. Its relatively high thermal neutron absorption cross section may necessitate increased fuel enrichment or thinner cladding geometry. In addition, it exhibits a lower melting point compared to zirconium-based alloys. Despite these limitations, the alloy's excellent mechanical strength provides design flexibility. However, the thermophysical properties of 42XNM remain uncharacterized in the open literature [14, 15].

2.2. Laser flash technique

The Laser Flash Technique (LFT) is a widely used experimental method to determine the thermal diffusivity of solid materials, especially at elevated temperatures. The principle of the technique involves subjecting one side of a thin disk-shaped sample to a short laser pulse, which causes a rapid temperature rise. The resulting temperature change on the opposite side of the sample is monitored over time, allowing the calculation of the thermal diffusivity of the material based on the rate of heat propagation [4, 5].

LFT offers several advantages, including noncontact heating, rapid measurement times, and applicability over a wide temperature range. Due to its precision and efficiency, LFT has become a standard method for thermal property characterization in materials research, including accident tolerant fuel cladding materials [4, 5].

In this study, two different instruments employing the laser flash technique were used, as described in the following subsections. Although both devices operate on the same fundamental principle, their technical configurations and measurement capabilities differ. Despite this, the sample preparation procedures were largely consistent.

2.2.1. Samples preparation

The main distinction in sample preparation was related to the nature of the material, specifically whether the sample was a metallic alloy or a ceramic silicon carbide (SiC)-based material. In the case of metallic alloys, the samples were cut with the high precision saw into smaller segments and then flattened into 10×10 mm square specimens using the hydraulic press. Detailed alloy preparation steps are illustrated in Figure 1.

For SiC-based samples, which are inherently brittle and not suitable for mechanical flattening, the final pressing step was omitted. as a result, the prepared SiC samples retained a slightly curved profile while maintaining comparable dimensions. This is shown in Figure 2.

2.2.2. NETZSCH LFA 427 Laser Flash apparatus

Most of the measurements were performed using the commercial NETZSCH LFA 427 apparatus, widely regarded as a state-of-the-ATF system to determine thermal diffusivity. This instrument is known for its high accuracy, repeatability, short measurement duration, and flexible sample holders, as well as the ability to perform measurements under various atmospheres. Depending on the furnace configuration, it covers a wide temperature range from 20 °C to 2 000 °C. In this study, only the 1 600 °C furnace was used due to the melting points of most materials and the technical limitations of the 2 000 °C unit [16].

The principle of operation is based on the laser flash method. A laser pulse heats the bottom surface of a sample held at an isothermal condition. The temperature rise on the upper surface is then recorded by an InSb infrared detector. The characteristic parameter, $t_{0.5}$, is the time required to reach half of the maximum temperature increase [16].

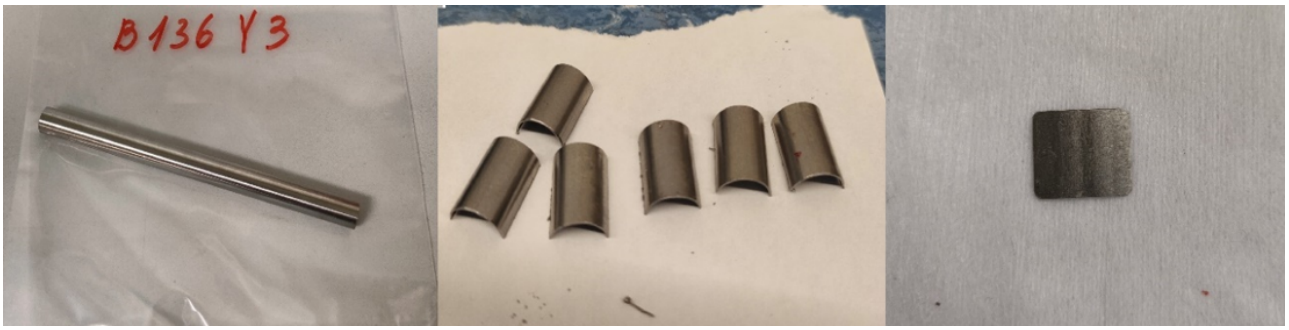

Figure 1. Preparation of alloy-based samples: on the left, the supplied specimen; in the center, the cut segments; and on the right, the final sample prepared for laser flash analysis.

Figure 2. Preparation of SiC samples: on the left, the supplied specimen; in the center, the cut segments; and on the right, the final sample prepared for laser flash analysis.

From the measured $t_{0.5}$ and known sample thickness l, the thermal diffusivity α is calculated using the standard Parker model [16]:

$$\alpha = \frac{0.1388 \cdot l^2}{t_{0.5}}$$

Before measurement, the samples were cleaned with ethanol and mounted in Al_2O_3 holders, then inserted into the furnace. A helium atmosphere was maintained by triple evacuation and purging, followed by a steady flow of 100 ml min^{-1} of He. Measurements were conducted from room temperature to near melting points in suitable increments, adjusted according to the behavior of thermal diffusivity.

2.2.3. Custom LFA setup developed at Karlsruhe

In addition to measurements performed with the commercial LFA NETZSCH system, a custom-built laser flash apparatus developed at JRC Karlsruhe was used, particularly for determining the melting points of materials with very high thermal stability, such as SiC-based samples. Unlike the commercial system, this setup is not limited by temperature and can operate in extremely high ranges under controlled conditions.

Unlike the NETZSCH device, the custom-built LFA apparatus at JRC Karlsruhe is configured horizontally. It follows the same fundamental principle: a laser pulse is directed at one side of the sample, and a pyrometer detects the emitted thermal radiation. The setup is enclosed in an argon-filled chamber to ensure an inert atmosphere and prevent oxidation during high-temperature testing. A photograph of the setup is presented in Figure 3.

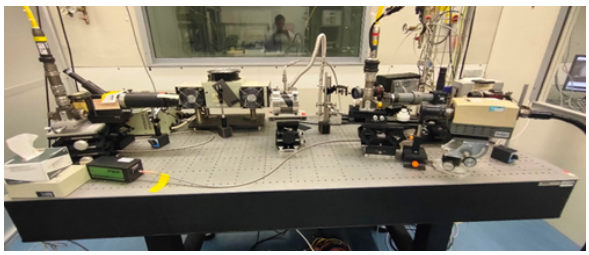

Figure 3. Custom LFA setup developed and operated at JRC Karlsruhe.

More detailed information on the configuration, measurement procedure and operational principles of the custom-built LFA system can be found in the study [17].

The sample preparation was identical to that used with the NETZSCH system: The surfaces were cleaned and placed in graphite holders. After calibration with a trigger pulse, measurements were made. Due to the lack of known emissivity values and limited spectrometric support, melting temperatures were estimated from cooling curves by identifying plateaus, which correspond to phase transitions.

3. Results

Thermal diffusivity data were measured across a wide temperature range using the laser flash technique. To ensure consistency and comparability, the same evaluation approach was applied to each material. The

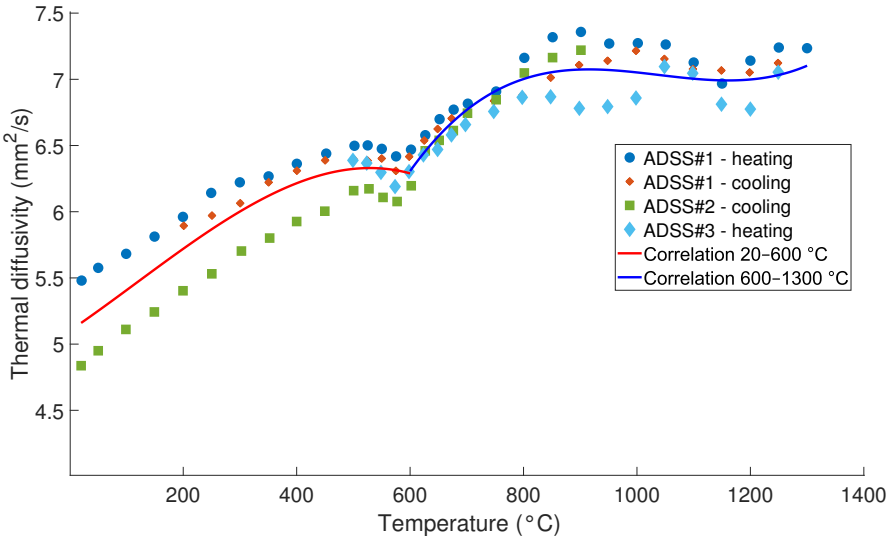

FIGURE 4. Thermal diffusivity of ADSS samples – measured data.

measured data were fitted using third-order polynomial functions and the fit quality was assessed through relative error. The relative error was determined as the deviation between the experimental data and the fitted curve, normalized to the measured value. In subsequent subsections, the results for each material are discussed individually, including thermal behavior, observed trends, and the accuracy of the fitted correlations.

3.1. High Aluminum Duplex Stainless Steel (ADSS #B51)

The measured thermal diffusivity values for all high-aluminum duplex stainless steel (ADSS) samples are summarized in Figure 4. The experimental data set comprises four measurement sequences conducted on three distinct specimens. Detailed sample information, including sample labels and thicknesses, is provided in Table 3. Measurements labeled as heating were obtained during continuous temperature increase, while those labeled as cooling were recorded during subsequent temperature decrease. The temperature range for each experiment was carefully selected with respect to the melting point of the material to prevent any phase transitions or thermal degradation.

Sample ID	Thickness [mm]
ADSS#1	3.110
ADSS#2	3.085
ADSS#3	3.133

TABLE 3. IDs ADSS#51 samples.

All three samples exhibit consistent thermal diffusivity behavior, with a distinct change in trend observed around 600 °C. This inflection point motivated the division of the data into two fitting intervals: 20–600 °C and 600–1 300 °C. The thermal diffusivity $\alpha(T)$ in $\mathrm{mm^2\,s^{-1}}$ for ADSS #51, evaluated as a function of temperature T (in °C), is described by the following third-order polynomial fits for temperature ranges 20–600 °C and 600–1 300 °C:

For T = 20–600 °C:

$$\alpha(T) = 5.101 + 2.909 \cdot 10^{-3} \cdot T + 2.164 \cdot 10^{-6} \cdot T^2 - 6.185 \cdot 10^{-9} \cdot T^3. \quad (1)$$

For T = 600–1 300 °C:

$$\alpha(T) = -5.068 + 3.599 \cdot 10^{-2} \cdot T - 3.516 \cdot 10^{-5} \cdot T^2 + 1.129 \cdot 10^{-8} \cdot T^3. \quad (2)$$

The relative errors for these fits are 3.47 % in the low-temperature range and 2.05 % in the high-temperature range, indicating good agreement between the fitted model and the experimental data.

3.2. FeCrAl B136Y3

The thermal diffusivity behavior of the FeCrAl B136Y3 alloy was also investigated using multiple measurements over a wide temperature range. The results, plotted in Figure 5, reveal a significant change in trend near 600 °C. Since thermal diffusivity depends inversely on the specific heat capacity c_p, anomalies in c_p directly affect α. For FeCrAl alloys, peaks in c_p are typically observed around 480–630 °C, originating from the magnetic contribution during the second order phase transition from the ferromagnetic state state to the paramagnetic state [18]. Based on this, the data were divided into two fitting intervals: 20–600 °C and 600–1 350 °C. Each segment was fitted with a third-order polynomial.

The dataset consists of multiple measurements conducted during both heating and cooling cycles on three independently prepared specimens. The measurements labeled *heating* correspond to continuous

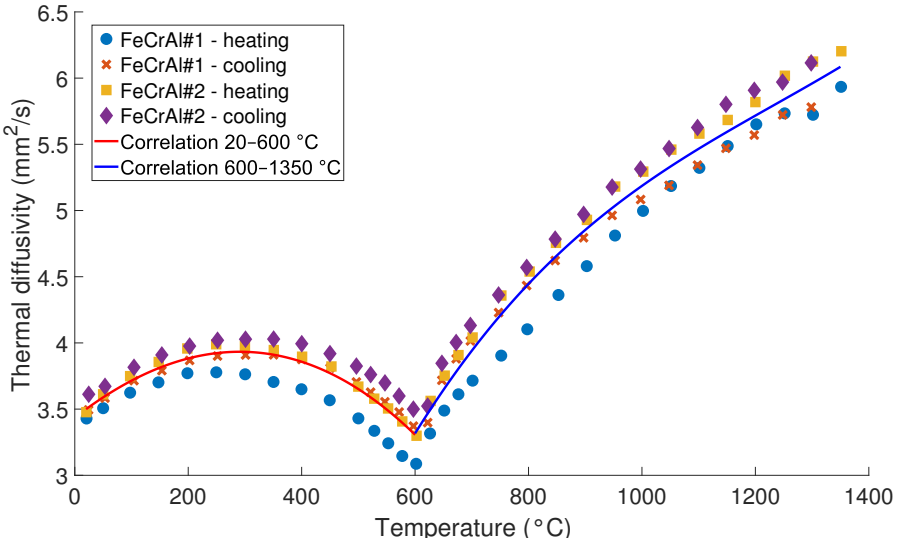

Figure 5. Thermal diffusivity of FeCrAl B136Y3.

increases in temperature, while *cooling* corresponds to the reverse process. The temperature limits were chosen with respect to the melting point of the alloy, ensuring thermal stability and preventing phase transitions or degradation. The measured sample thicknesses are provided in Table 4.

Sample ID	Thickness [mm]
FeCrAl#1	0.404
FeCrAl#2	0.384
FeCrAl#3	0.384

Table 4. IDs FeCrAl B136Y3 samples.

The thermal diffusivity $\alpha(T)$, in $\mathrm{mm^2\,s^{-1}}$, as a function of temperature T (in °C), is expressed by the following polynomial equations:

For $T = 20$–$600\,°\mathrm{C}$:

$$\alpha(T) = 3.4357 + 3.3245 \cdot 10^{-3} \cdot T - 5.2211 \cdot 10^{-6} \cdot T^2 - 1.1306 \cdot 10^{-9} \cdot T^3. \quad (3)$$

For $T = 600$–$1\,350\,°\mathrm{C}$:

$$\alpha(T) = -4.1950 + 1.9468 \cdot 10^{-2} \cdot T - 1.3822 \cdot 10^{-5} \cdot T^2 + 3.7349 \cdot 10^{-9} \cdot T^3. \quad (4)$$

The relative fitting errors are 2.50 % for the lower range and 3.03 % for the higher temperature range, indicating good agreement with the measured data and validating the polynomial approach used for the prediction of thermal diffusivity.

3.3. SiC CTP

The measured thermal diffusivity values for SiC CTP samples are summarized in Figures 6 and 7. Unlike metallic materials such as ADSS or FeCrAl, SiC is characterized by an exceptionally high melting point approaching 3 000 °C. To cover the broad temperature range required for accurate characterization, two laser flash analysis (LFA) systems were employed: the commercial NETZSCH LFA 427 for measurements in the lower-temperature regime, and a custom-built high-temperature LFA system operated at JRC Karlsruhe for the extended range.

Detailed sample specifications are listed in Table 5. All measurements were conducted under an inert argon atmosphere to avoid oxidation at elevated temperatures.

Sample ID	Thickness [mm]
CTP#1	1.000
CTP#2	0.976
CTP#3	0.967

Table 5. IDs SiC CTP samples.

The thermal diffusivity $\alpha(T)$ in $\mathrm{mm^2\,s^{-1}}$, as a function of temperature T (in °C), was fitted using third-order polynomial regressions. The results are described by the following equations:

For $T = 20$–$1\,550\,°\mathrm{C}$:

$$\alpha(T) = 5.8770 - 5.5201 \cdot 10^{-3} \cdot T + 4.4874 \cdot 10^{-6} \cdot T^2 - 1.3550 \cdot 10^{-9} \cdot T^3. \quad (5)$$

This correlation was obtained using data from the NETZSCH apparatus and shows a relative error of 9.3 %, indicating high consistency with the experimental observations.

For $T = 1\,200$–$2\,350\,°\mathrm{C}$:

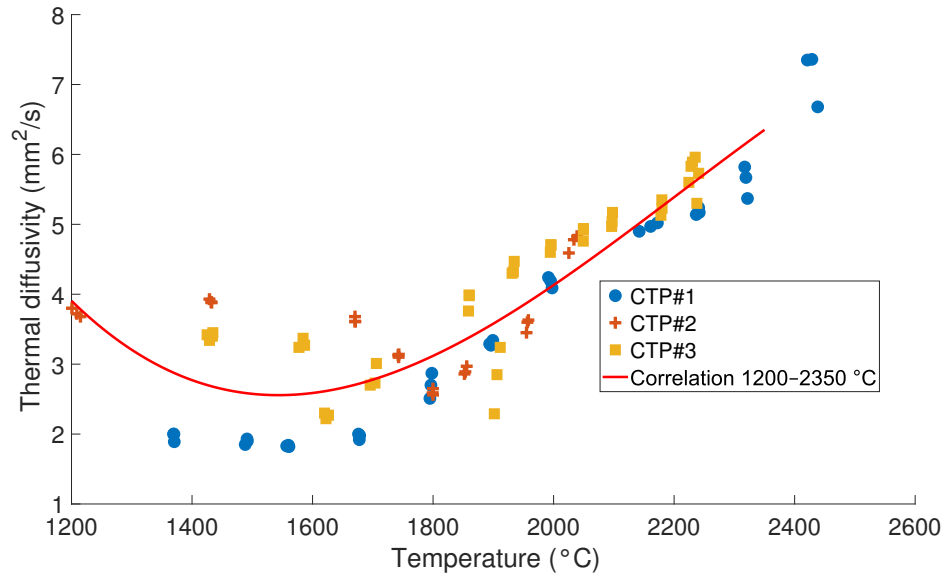

FIGURE 6. Thermal diffusivity of CTP using Custom LFA Setup Developed at Karlsruhe.

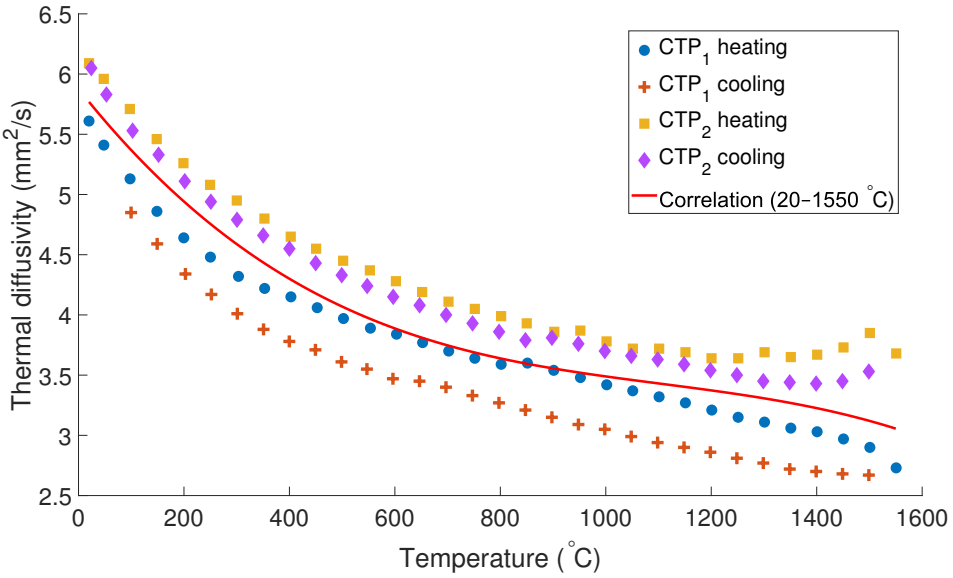

FIGURE 7. Thermal diffusivity of SiC CTP using NETZSCH 427.

$$\alpha(T) = 43.815 - 6.5121 \cdot 10^{-2} \cdot T + 3.2423 \cdot 10^{-5} \cdot T^2 - 4.8918 \cdot 10^{-9} \cdot T^3. \quad (6)$$

The fit based on high-temperature measurements from the custom-built LFA exhibits a higher relative error of 15.47 %, reflecting the increased experimental uncertainty at extreme temperatures.

Overall, the thermal diffusivity in SiC CTP initially exhibits a decreasing trend with increasing temperature, which is typical for ceramic materials and is attributed to enhanced phonon scattering. However, the data obtained at higher temperatures reveal a noticeable change in this behavior: Around 1 800 °C, the thermal diffusivity begins to increase. Such an increase cannot be explained solely by the temperature dependence of λ, c_p, or ρ, which would all lead to a continued decrease in α [8].However, for such high temperatures, the available data are insufficient. The observed deviation is therefore likely related to microstructural effects specific to the multilayer SiC/SiC architecture, such as the formation of microcracks, changes in the interfaces between layers, or enhanced radiative heat transfer at elevated temperatures. These mechanisms can alter the effective heat transport and may contribute to the apparent increase in α observed in the high-temperature regime.

3.4. SiC NITE

The thermal diffusivity of the NITE composite was determined over an extended temperature range using two different experimental setups. Measurements up

to approximately 1 575 °C were performed on the commercial LFA NETZSCH system, while measurements at higher temperatures were performed using a custom-built LFA device developed at JRC Karlsruhe. This dual instrument approach was necessary because of the elevated melting point of the material and to obtain as many data as possible. Also, since second-grade samples were used, some variability between samples is expected. This is reflected in the measured values, where two distinct trends are consistently observed, one with slightly higher diffusivity and the other with lower diffusivity. These variations were addressed by fitting separate polynomial models to each trend.

A third-order polynomial correlation was fitted to the data in the low and medium temperature range (20–1 575 °C) obtained from the NETZSCH instrument. The thermal diffusivity α(T) in $\mathrm{mm^2\,s^{-1}}$ as a function of the temperature T at °C is given by:
Thermal diffusivity correlations for NITE samples measured by LFA NETZSCH (20–1 575 °C):

Low variant:

$$\alpha(T) = 24.5006 - 4.3192 \cdot 10^{-2} \cdot T + 3.7750 \cdot 10^{-5} \cdot T^2 - 1.1777 \cdot 10^{-8} \cdot T^3. \quad (7)$$

The relative deviation of this fit is 5.38 %, indicating a good agreement between the model and the measured values.

High variant:

$$\alpha(T) = 31.0209 - 5.3337 \cdot 10^{-2} \cdot T + 4.5939 \cdot 10^{-5} \cdot T^2 - 1.4189 \cdot 10^{-8} \cdot T^3. \quad (8)$$

This approximation yields a relative error of 4.46 %, confirming the reliability of the fit across the evaluated temperature range.

For temperatures exceeding the upper measurement limit of the commercial LFA (above 1 600 °C), a second dataset was acquired using the custom-made LFA system, allowing measurements up to 2 400 °C. The corresponding polynomial fit for this high temperature range is expressed as follows.
Thermal diffusivity correlations for NITE samples measured by custom LFA (JRC Karlsruhe):

Low variant 1 080–2 110 °C:

$$\alpha(T) = -23.2719 + 5.4946 \cdot 10^{-2} \cdot T - 3.5958 \cdot 10^{-5} \cdot T^2 + 7.5407 \cdot 10^{-9} \cdot T^3. \quad (9)$$

The relative error of this fit is 2.41 %, demonstrating a very good agreement with the measured data.

High variant 1 120–2 420 °C:

$$\alpha(T) = -5.8084 + 2.6730 \cdot 10^{-2} \cdot T - 1.7708 \cdot 10^{-5} \cdot T^2 + 3.5280 \cdot 10^{-9} \cdot T^3. \quad (10)$$

The relative error of this fit is 2.89 %, confirming a very good agreement between the fitted model and the experimental data.

The relative error of this approximation is 2.89 %, which remains within acceptable bounds for high-temperature measurements involving ceramic-metal composites.

Overall, the diffusivity of NITE exhibits a general decreasing trend with increasing temperature in the lower regime, which is characteristic of phonon-dominated heat transport in composite materials. Interestingly, data from the high temperature range suggest a less pronounced decline and even a possible stabilizing or increasing tendency above 2 000 °C. This behavior may reflect changes in microstructural dynamics or enhanced radiative contributions at extreme temperatures. More detailed analysis would be required to confirm these mechanisms.

All measured values, sample identifiers, and thicknesses are listed in Table 6. The thermal diffusivity results obtained from both the commercial LFA NETZSCH instrument and the custom-built LFA system developed at JRC Karlsruhe are presented in Figures 8 and 9.

Sample ID	**Thickness [mm]**
NITE#1	0.980
NITE#2	1.192
NITE#3	0.982

Table 6. IDs SiC NITE samples.

3.5. Cr-Ni alloy 42XNM

The thermal diffusivity of the material exhibits a clear trend change near 800 °C. To reflect this behavior, the data were divided into two temperature intervals: 20 to 800 °C and 800 to 1 275 °C, with each region fitted separately using third-order polynomial functions. This approach leads to a significantly improved fit and better captures the distinct regimes observed in the experimental data. The thermal diffusivities of 42XNM samples are summarized in Figure 10.

The data set comprises multiple measurements obtained from both heating and cooling cycles, performed on several independently prepared specimens. The distinction between heating and cooling measurements allows for the evaluation of potential hysteresis effects. The chosen temperature limits ensure that the analysis covers the most relevant range for the material without exceeding limits that could induce phase changes or sample degradation. Sample thicknesses can be found in Table 7.

For the lower temperature range (20–800 °C), the thermal diffusivity $\alpha(T)$ in $\mathrm{mm^2\,s^{-1}}$ is almost linear and can be described by the following correlation:

For T = 20–800 °C:

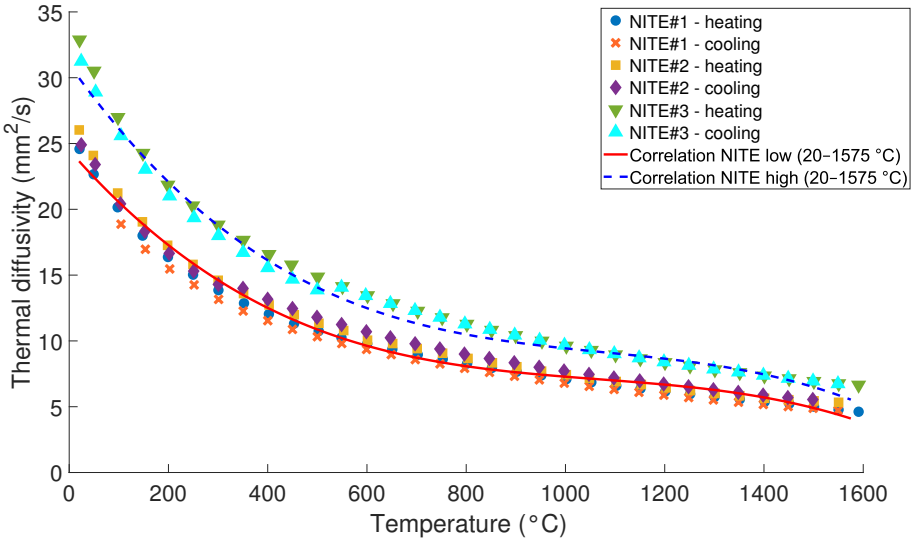

FIGURE 8. Thermal diffusivity of NITE CTP using NETZSCH 427.

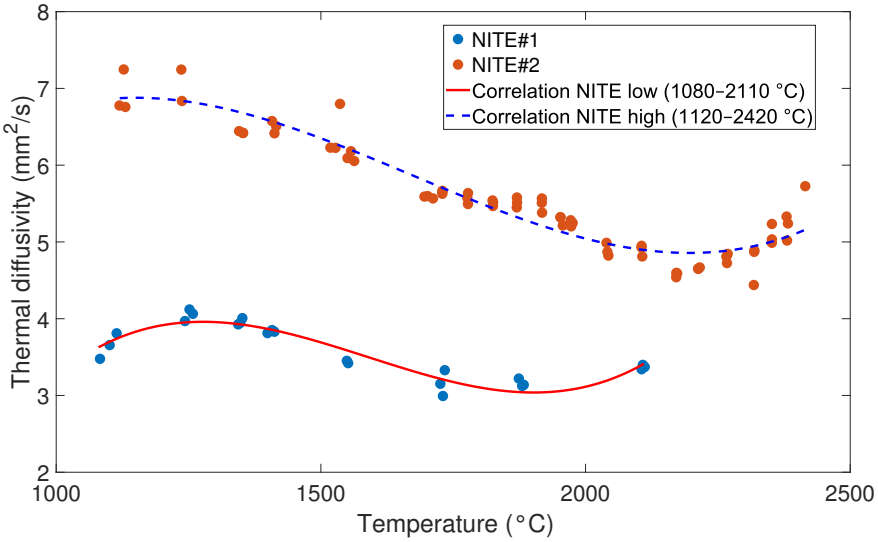

FIGURE 9. Thermal diffusivity of NITE using Custom LFA Setup Developed at Karlsruhe.

Sample ID	Thickness [mm]
42XNM#1	0.590
42XNM#2	0.574
42XNM#3	0.582

TABLE 7. IDs 42XNM samples.

$$\alpha(T) = 2.6628 + 4.5114 \cdot 10^{-3} \cdot T - 1.7916 \cdot 10^{-6} \cdot T^2 + 5.9649 \cdot 10^{-10} \cdot T^3. \quad (11)$$

The relative deviation for this correlation is 1.64 %, indicating a very good agreement between the model and the experimental data in the lower temperature region.

For the higher temperature region (800–1 275 s^{-1}C), the best-fit polynomial is:

For T = 800–1 275 °C:

$$\alpha(T) = 24.2494 - 6.1083 \cdot 10^{-2} \cdot T + 6.4129 \cdot 10^{-5} \cdot T^2 - 2.1474 \cdot 10^{-8} \cdot T^3. \quad (12)$$

The relative error in this interval is 2.42 %, confirming a reliable fit even in the elevated temperature regime. The combined correlations reflect the characteristic behavior of Cr-Ni alloys at elevated temperatures and provide a reliable basis for the thermal diffusivity.

4. CONCLUSIONS

This study investigated the thermal diffusivity of five advanced ATF cladding candidates using the Laser Flash Technique across a wide temperature range. The

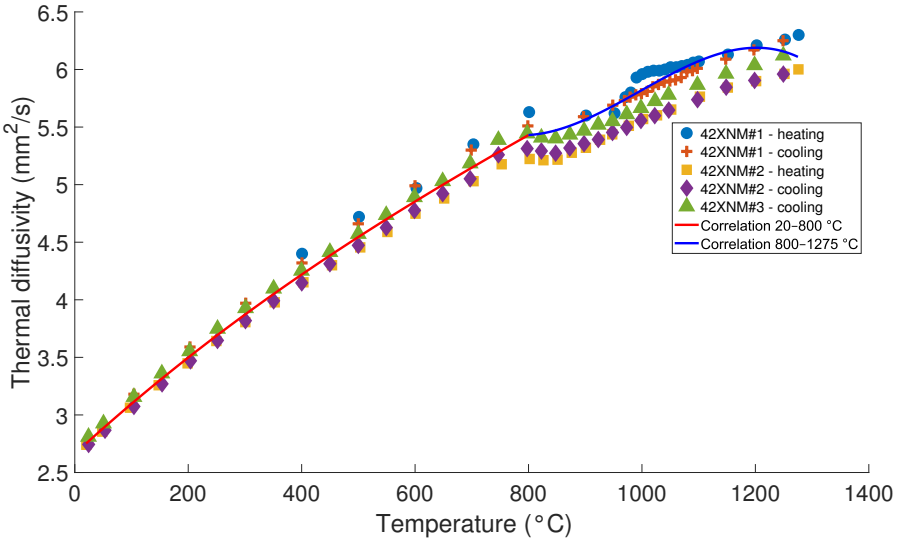

Figure 10. Thermal diffusivity of 42XNM using NETZSCH 427.

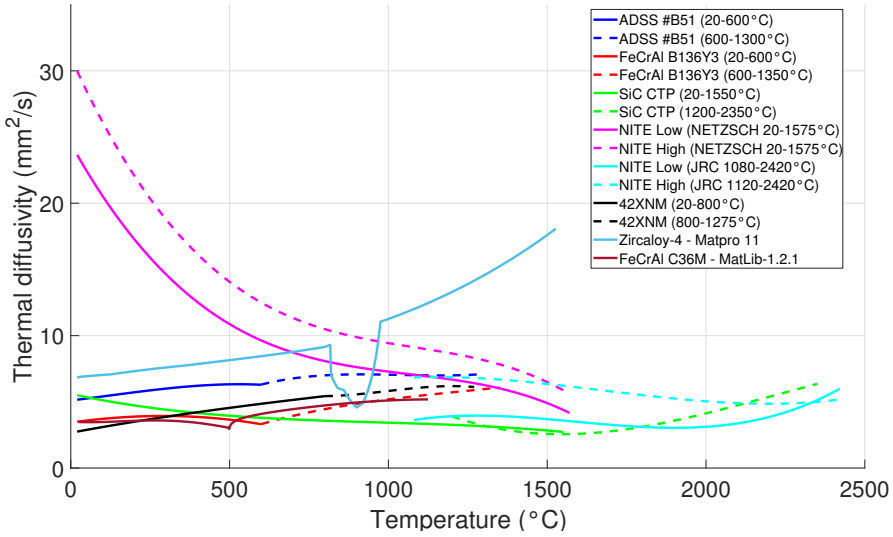

Figure 11. Overview of thermal diffusivity correlations for advanced ATF claddings, including Zircaloy-4 as a reference.

measured data reveal distinct temperature-dependent behavior for each material, driven by their unique microstructures and compositions.

Figure 11 shows all the thermal diffusivity correlations obtained, including the calculated curve for Zircaloy-4 based on the MATPRO database and FeCrAl C36M with a composition similar to FeCrAl B136Y3 from MatLib-1.2.1 [19], allowing a direct comparison of these alloys with other advanced cladding materials. It is evident that the thermal diffusivity of the various zirconium alloys does not differ significantly among themselves. The sharp drop observed in the Zircaloy-4 curve is a consequence of using the Matpro 11 database, where the thermal diffusivity values are calculated based on a formula that incorporates a stepwise change in the heat capacity (cp) due to the α-to-β phase transformation. However, in reality, this transition is much smoother, and the actual thermal diffusivity curve should is continuous, without such an abrupt decrease.

All metallic materials (ADSS # B51, FeCrAl B136Y3 and Cr-Ni alloy 42XNM) exhibit a typical increase in thermal diffusivity with increasing temperature due to enhanced phonon scattering, with inflection points observed between 600 and 800 °C due to phase transformations. Third-order polynomial fits provided an accurate modeling of this trend, with relative deviations below 6.8 %.

For ceramic materials (SiC CTP and SiC NITE), the measurements were extended to 2 400 °C, enabled by a custom-built high temperature LFA system. Both materials showed expected decreasing trends in thermal diffusivity at lower temperatures. However, a change in behavior was observed at elevated

temperatures, especially for SiC CTP, where the thermal diffusivity begins to rise above 1 800 °C reaching highest values close to its melting point. These trends were successfully captured by fitting correlations with acceptable relative errors.

In addition, the correlations obtained using the NETZSCH and the custom LFA Setup at JRC Karlsruhe show only minor differences in the resulting thermal diffusivity values. These discrepancies are not significant and can probably be attributed to differences in measurement technique or instrument calibration. Slight variations may also arise from different sample preparation or environmental conditions during the measurements, but overall, the agreement between both sets of data confirms the reliability of the results.

In general, the presented correlations provide reliable insight into the thermal diffusivity behavior of advanced cladding materials across a broad temperature range. Among the evaluated materials, only SiC NITE demonstrates noticeably higher thermal diffusivity values compared to Zr-based alloys in the initial part of the temperature interval, up to approximately 700 °C for the 'low' correlation and up to 900 °C for the 'high' correlation. However, beyond these temperatures, none of the candidate materials maintains a significant advantage, and their thermal diffusivity values become comparable to or even lower than those of conventional zirconium alloys [20].

Acknowledgements

We acknowledge the state support of the Technology Agency of the Czech Republic within the National Competence Centre Programme II, project TN02000012 „Center of Advanced Nuclear Technology II".

JRC is not an author/co-author: The experimental data used in this research were generated through access to the JRC-Karlsruhe actuslab research infrastructure under the Framework for access to the Joint Research Centre physical Research Infrastructures of the European Commission (Call 2022-2-RD-Actuslab FMR "ADULATOR" aUL-271 "ADvanced fUeLs and maTerials prOpeRties" project, Research Infrastructure access agreement N°36618/01). Any opinions, findings, conclusions, or recommendations expressed in this document are those of the authors and do not necessarily reflect those of the European Commission.

References

[1] K. A. Terrani. Accident tolerant fuel cladding development: Promise, status, and challenges. *Journal of Nuclear Materials* **501**:13–30, 2018. https://doi.org/10.1016/j.jnucmat.2017.12.043

[2] B. A. Pint, K. A. Terrani, M. P. Brady, et al. High temperature oxidation of fuel cladding candidate materials in steam-hydrogen environments. *Journal of Nuclear Materials* **440**(1):420–427, 2013. https://doi.org/10.1016/j.jnucmat.2013.05.047

[3] M. Khatib-Rahbar, A. Krall, Z. Yuan, M. Zavisca. Review of accident tolerant fuel concepts with implications to severe accident progression and radiological releases. Tech. Rep. ERI/NRC 20-209, Energy Research, Inc., 2020. [2024-04-15]. https://adamswebsearch2.nrc.gov/webSearch2/main.jsp?AccessionNumber=ML20287A477

[4] W. J. Parker, R. J. Jenkins, C. P. Butler, G. L. Abbott. Flash method of determining thermal diffusivity, heat capacity, and thermal conductivity. *Journal of Applied Physics* **32**(9):1679–1684, 1961. https://doi.org/10.1063/1.1728417

[5] K. D. Maglić, R. E. Taylor. The apparatus for thermal diffusivity measurement by the laser pulse method. In K. D. Maglić, A. Cezairliyan, V. E. Peletsky (eds.), *Compendium of Thermophysical Property Measurement Methods: Volume 2*, pp. 281–314. Springer US, Boston, MA, 1992. https://doi.org/10.1007/978-1-4615-3286-6_10

[6] H. Kim, H. Jang, G. O. Subramanian, et al. Development of alumina-forming duplex stainless steels as accident-tolerant fuel cladding materials for light water reactors. *Journal of Nuclear Materials* **507**:1–14, 2018. https://doi.org/10.1016/j.jnucmat.2018.04.027

[7] C. Kim, C. Tang, M. Große, M. Steinbrück. Oxidation kinetics of nuclear-grade FeCrAl alloys in steam in the temperature range 600–1500 °C. In *Proceedings of TOPFUEL 2021 Conference*, pp. 1–10. Santander, Spain, 2021.

[8] B. Qiu, J. Wang, Y. Deng, et al. A review on thermohydraulic and mechanical-physical properties of SiC, FeCrAl and Ti3SiC2 for ATF cladding. *Nuclear Engineering and Technology* **52**(1):1–13, 2020. https://doi.org/10.1016/j.net.2019.07.030

[9] C. Kim, C. Tang, M. Grosse, et al. Oxidation mechanism and kinetics of nuclear-grade FeCrAl alloys in the temperature range of 500–1500 °C in steam. *Journal of Nuclear Materials* **564**:153696, 2022. https://doi.org/10.1016/j.jnucmat.2022.153696

[10] P. Aragón, F. Feria, L. E. Herranz. Modelling FeCrAl cladding thermo-mechanical performance. Part I: Steady-state conditions. *Progress in Nuclear Energy* **153**:104417, 2022. https://doi.org/10.1016/j.pnucene.2022.104417

[11] J. Halfinger, D. Rogers, F. Mohammadi. Multilayer silicon carbide composite material technology for high-temperature concentrated solar–thermal power components. DOE Receiver & Reactor Workshop, 2021. [2025-04-28]. https://www.energy.gov/sites/default/files/2024-02/4.4%20JeffHalfinger_CTP_ceramicTubes_0.pdf

[12] J.-S. Park, N. Nakazato, N. Takayama, et al. High speed formation of pyro-carbon coat on silicon carbide fiber by continuous chemical vapor deposition furnace. *Fusion Engineering and Design* **125**:442–446, 2017. https://doi.org/10.1016/j.fusengdes.2017.05.031

[13] A. Kohyama, S. Konishi, A. Kimura. Fusion materials and fusion engineering R & D in Japan. *Nuclear Engineering and Technology* **37**:423–432, 2005.

[14] B. A. Gurovich, A. S. Frolov, E. A. Kuleshova, et al. Microstructural evolution of the 42XNM alloy during a severe accident (LOCA). *Journal of Nuclear Materials* **561**:153535, 2022. https://doi.org/10.1016/j.jnucmat.2022.153535

[15] B. A. Gurovich, A. S. Frolov, I. V. Fedotov. Improved evaluation of ring tensile test ductility applied to neutron irradiated 42XNM tubes in the temperature range of (500–1100) °C. *Nuclear Engineering and Technology* **52**(6):1213–1221, 2020. https://doi.org/10.1016/j.net.2019.11.019

[16] NETZSCH-Gerätebau GmbH. *LFA 427 – High Temperature Laser Flash Apparatus*, 2020. [2025-04-28]. https://analyzing-testing.netzsch.com/_Resources/Persistent/7/d/0/5/7d05af00d326ac6649fdbde0a7fac6925b0c6097/LFA_427_en_web.pdf

[17] T. Pavlov, L. Vlahovic, D. Staicu, et al. A new numerical method and modified apparatus for the simultaneous evaluation of thermo-physical properties above 1500K: A case study on isostatically pressed graphite. *Thermochimica Acta* **652**:39–52, 2017. https://doi.org/10.1016/j.tca.2017.03.004

[18] K. G. Field, M. A. Snead, Y. Yamamoto, K. A. Terrani. Handbook on the material properties of FeCrAl alloys for nuclear power production applications. Tech. Rep. ORNL/TM-2017/186 Rev. 1, Oak Ridge National Laboratory, 2017. [2025-04-29]. https://info.ornl.gov/sites/publications/Files/Pub114121.pdf

[19] K. J. Geelhood, W. G. Luscher, L. Kyriazidis, et al. Matlib-1.2.1: Nuclear material properties library. Technical Report PNNL-35702, Pacific Northwest National Laboratory, Richland, Washington, 2024. Prepared for the U.S. Nuclear Regulatory Commission, Office of Nuclear Regulatory Research. [2025-04-29]. https://www.nrc.gov/docs/ML2417/ML24177A228.pdf

[20] D. L. Hagrman, G. A. Reymann. MATPRO-Version 11: a handbook of materials properties for use in the analysis of light water reactor fuel rod behavior. Tech. rep., Idaho National Laboratory, 1979. https://doi.org/10.2172/6442256